Published in final edited form as:
Nature. 2014 March 6; 507(7490): 68–72. doi:10.1038/nature13116.

Molecular basis of nitrate uptake by the plant nitrate transporter NRT1.1

Joanne L. Parker[1] and **Simon Newstead**[1,2]

[1]Department of Biochemistry, University of Oxford, Oxford, OX1 3QU, UK

[2]Research Complex at Harwell, Rutherford Appleton Laboratory, Didcot, UK

Summary

The NRT1/PTR family of proton-coupled transporters are responsible for nitrogen assimilation in eukaryotes and bacteria through the uptake of peptides. However, in the majority of plant species members of this family have evolved to transport nitrate as well as additional secondary metabolites and hormones. In response to falling nitrate levels, NRT1.1 is phosphorylated on an intracellular threonine that switches the transporter from a low to high affinity state. Here we present both the apo and nitrate bound crystal structures of *Arabidopsis thaliana* NRT1.1, which together with *in vitro* binding and transport data identify a key role for His356 in nitrate binding. Our data support a model whereby phosphorylation increases structural flexibility and in turn the rate of transport. Comparison with peptide transporters further reveals how the NRT1/PTR family has evolved to recognize diverse nitrogenous ligands, whilst maintaining elements of a conserved coupling mechanism within this superfamily of nutrient transporters.

Nitrogen is a key element in biology, required for the synthesis of amino and nucleic acids and is a fundamental nutrient for cellular metabolism. The PTR or peptide transporter family, also known as the POT, or proton dependent oligopeptide transporter family, plays an important role in nitrogen assimilation in bacteria, fungi and mammals through the uptake of short peptides from the environment [1,2]. In contrast, in the majority of plant species nitrogen is largely obtained through the uptake of nitrate (NO_3^-) from the soil [3]. This is achieved through the actions of specific nitrate transporters in the plasma membrane of root cells [4] and is controlled through the NRT1 and NRT2 gene families that encode for low (K_M mM) and high (K_M μM) affinity transporters respectively [5,6]. Intriguingly the NRT1 family of nitrate transporters phylogenetically belongs to the PTR family, and may have evolved from an ancestral peptide transport protein [7].

In plants the NRT1/PTR family, recently renamed the NPF (NRT1/PTR Family) [8], has functionally diverged with individual members recognizing peptides, glucosinolate defense compounds, plant hormones or nitrate [9-12]. The NRT1/PTR family belongs to the Major Facilitator Superfamily (MFS) of secondary active transporters [13,14] that use the proton electrochemical gradient to drive substrate uptake into the cell [15-17]. MFS transporters

Correspondence and requests for materials should be addressed to JLP (joanne.parker@bioch.ox.ac.uk) or SN (simon.newstead@bioch.ox.ac.uk).

Author Contributions. JLP & SN designed, performed and analyzed all experiments and wrote the manuscript.

The atomic coordinates and structure factors of the apo and nitrate bound *At*NRT1.1 are deposited in the Protein Data Bank with accession codes 4cl4 and 4cl5 respectively.

The authors declare no competing financial interests.

Readers are welcome to comment on the online version of the paper.

Europe PMC Funders Author Manuscripts

operate via an alternating access mechanism wherein a centrally located binding site is re-orientated to either side of the membrane to uptake and release substrate [18-20]. Recent crystal structures of bacterial members of the NRT1/PTR family have identified pairs of salt bridges that orchestrate the orientation of the transporter and revealed proton binding residues that are conserved across the family from pro- to eukaryotes [21,22]. An important question therefore is how the binding site in this transporter family has evolved to recognize and transport diverse molecules while retaining elements of the same coupling mechanism.

The *Arabidopsis thaliana* nitrate transporter, *At*NRT1.1 (*At*NPF6.3), is the founding member [7] of the NRT1/PTR family of transporters and shares significant sequence identity to mammalian and bacterial PTR peptide transporters (Extended Data Fig. 1). Interestingly *At*NRT1.1 has two K_M values for nitrate [23]; in conditions of high nitrate availability (> 1mM) *At*NRT1.1 behaves as a low-affinity transporter (K_M ~ 4 mM). However, when nitrate levels fall below 1mM, *At*NRT1.1 is switched into a high-affinity mode (K_M ~ 40 μM). This switch occurs following phosphorylation of an intracellular threonine, Thr101, by the kinase CIPK23 [24]. This regulatory mechanism allows for the rapid adaption to changing nitrate levels before the dedicated high affinity transporter family is expressed [25]. These observations suggest a complex interplay between transporter activity and post-translational modification at the molecular level that currently has no structural or biochemical basis for explanation.

Structural basis of nitrate recognition in *At*NRT1.1

To study the binding of nitrate to *At*NRT1.1 we developed a microscale thermophoresis assay [26,27] (Extended Data Fig. 2a) and determined the K_D for nitrate to be 1 ± 0.15 mM (Fig. 1a & Extended Data Fig. 2). A wide range of nitrate concentrations were tested (1 μM – 50 mM) and we did not observe a high affinity state. We further tested a range of different ligands and show that *At*NRT1.1 specifically recognizes both nitrate and chlorate, a herbicide for which the *At*NRT1.1 protein was originally named (Chlorate Resistance 1) [7] but does not recognize nitrite, alanine, sulphate, phosphate or the di-peptide Ala-Ala (Extended Data Fig. 2c). A key question surrounding the function of *At*NRT1.1 is the switch between high and low affinity states. Using the phosphomimetic variant Thr101Asp, we investigated the effect on nitrate binding. The K_D for nitrate binding to the Thr101Asp was the same as WT (K_D 1 ± 0.12 mM) (Fig. 1a), suggesting that phosphorylation is unlikely to directly alter the nitrate-binding site. To follow up this finding and identify the nitrate-binding site we crystallised *At*NRT1.1 in the presence and absence of nitrate. The crystal structures were determined to 3.7 Å (Extended Data Table 1).

The apo structure of *At*NRT1.1 contains 12 transmembrane (TM) spanning alpha helices, consisting of N-(TM1-TM6) and C-terminal (TM7-TM12) bundles forming the canonical MFS fold (Fig. 1b). Separating these two bundles is a previously uncharacterized intracellular domain consisting of 84 amino acids. This domain is predominantly alpha helical and extends outwards from the transporter domain at an approximate 90° angle, which we have termed the lateral helix (Fig. 1c). At the distal end of this helix are three conserved positively charged residues that may help to stabilize this domain on the intracellular side of the membrane. It is unlikely this domain is a crystallographic artifact as it does not make any crystal contacts and is sufficiently mobile that we cannot model residues 270-325. *At*NRT1.1 crystallizes as a dimer in the asymmetric unit cell, despite being monomeric in solution (Extended Data Fig. 3). The dimer interface forms between TM3 and TM6 of monomer A packing against the equivalent helices in monomer B and stabilized by hydrophobic interactions (Extended Data Fig. 3). The buried surface area between the two monomers is ~ 2136 Å2 and may be physiologically significant as both monomers are in the same orientation. Both monomer A and B adopt the same inward open

conformation (with an r.m.s.d. between monomer A and B of ~ 0.69 Å for 472 Cα atoms) with a clearly defined cavity extending outward from the middle of the protein towards the intracellular side of the membrane. Surprisingly the cavity is much larger than expected given the size of nitrate, being ~ 21 × 18 × 17 Å in diameter (Fig. 2a). The extracellular side of the binding site is tightly sealed through the packing together of TMs1-2 against TMs7-8. These helices form the extracellular gate in MFS transporters, which control access to the binding site from the outside of the cell [19,28,29]. Interestingly there exist no salt bridge interactions between these helices, unlike the prokaryotic NRT1/PTR homologues [14,21,22,30], instead the extracellular gate is stabilized through extensive hydrophobic interactions (Extended Data Fig. 4).

The nitrate bound structure was unchanged from the apo state with an r.m.s.d. of ~ 0.44 $Å^2$ for 472 C_α atoms. However, we observed a significant (> 3 sigma) mFo-DFc difference electron density peak within the central cavity, which we observed in crystals grown in the presence of nitrate. We therefore modeled nitrate into this density (Fig. 2 a & b & Extended Data Fig. 5). The nitrate molecule sits approximately 2.8 Å away from His356 on TM7; given the pH of the crystallization condition was 4.5 His356 is likely to be protonated and forming an electrostatic interaction with nitrate. An additional interaction via a hydrogen bond occurs with Thr360 on TM7, which sits approximately 2.9 Å away at the apex of the binding site. The binding of nitrate through an electrostatic interaction is similar but not identical to the recent crystal structure of NarU, a member of the biochemically distinct Nitrate Nitrite Porter (NNP) family, where two conserved arginine residues act to coordinate nitrate through hydrogen bonds (Extended Data Fig. 6) [31]. The other possible sites of interaction for nitrate therefore could be either Arg45 (TM1) and/or Lys164 (TM4). We mutated all three of these positively charged residues to alanine, however mutation of only His356 resulted in complete loss of nitrate binding, indicating an essential role of His356 in *At*NRT1.1 (Fig. 2c).

Substrate specificity in the NRT1/PTR family

As discussed previously, members of the NRT1/PTR family can transport peptides, nitrate and in the case of plant members, hormones and metabolites. A key question we wished to address was how the binding site of *At*NRT1.1 differed to that of the peptide transporters. Comparison with the binding site from the bacterial peptide transporter from *Shewanella oniendensis*, $PepT_{So}$, reveals that the two binding sites are strikingly similar (Fig. 2d). The previously identified ExxERF motif on TM1, which plays an important role in coupling proton binding to peptide transport [22] is present in the same position, as are Lys164 (TM4) and Glu476 (TM10). As predicted for their bacterial counterparts [21,22] Lys164 and Glu476 are likely to interact via a salt bridge in the outward facing conformation and form an important link between the N and C terminal bundles during transport (Extended Data Fig. 7).

Our comparison suggests the mechanism required for coupling proton movement to structural changes during transport is conserved regardless of substrate specificity. It is known the stoichiometry of *At*NRT1.1 and mammalian peptide transporters is at least 2:1 proton:nitrate, as transport is electrogenic [7,32]. It is therefore conceivable the ExxERF motif couples one proton, leaving His356 on TM7 to bind another proton and nitrate. In peptide transporters the equivalent region on TM7 has been shown to couple proton binding to peptide recognition [22] through an acidic residue, Asp316 in $PepT_{So}$. One major difference between the binding sites is the absence of an obvious salt bridge connecting the extracellular gate helices TM1 and TM7. Indeed in $PepT_{So}$ the arginine of this salt bridge occupies the same position in the protein as the nitrate (Figure 2c & d). Another significant difference is the replacement of the two conserved aromatic residues on TM1 (Phe28,

Tyr29), which are responsible for peptide specificity [21] with residues containing smaller side chains helping to create space for nitrate to bind. Given that di-peptides are coordinated horizontally between the N- and C-terminal bundles [22,30], it is conceivable that the increased width of the cavity in *At*NRT1.1 can no longer coordinate the amino and carboxy termini simultaneously. Coupled with the absence of the salt bridge and tyrosines, which help position the peptide and coordinate movement of TM1 and TM7, these seemingly esoteric alterations could explain why *At*NRT1.1 cannot recognize or transport peptides. 7

Functional role of phosphorylation at Thr101

Our structures show that Thr101 is situated at the bottom of TM3 and points towards a hydrophobic pocket constructed from residues in TM1 and TM4 (Fig. 3a). Given the position of Thr101 it is highly likely that phosphorylation would cause localized structural distortion in the packing of TM3 with TM1 and TM4 on the intracellular side of the protein. Consistent with this hypothesis we discovered that the Thr101Asp variant of *At*NRT1.1 was significantly less stable compared to WT protein (9 °C lower melting temperature) (Fig. 3b). To investigate the effect of the Thr101Asp substitution on nitrate uptake we reconstituted *At*NRT1.1 into liposomes and monitored the relative uptake of nitrate as a function of proton movement using a pH sensitive fluorophore (Extended Data Fig. 8). As *At*NRT1.1 is a proton coupled nitrate transporter this assay provides a reliable readout for nitrate transport. We discovered that compared to the WT protein, the Thr101Asp variant showed increased uptake of ~ 2.8 fold, whereas the His356Ala variant showed no detectable transport, consistent with an essential role in nitrate recognition (Fig. 3c).

Given the high sequence conservation of the N-terminal bundle within the NRT1/PTR family (Extended Data Fig. 1 & 9a), we mutated the equivalent threonine in $PepT_{So}$ (Thr87) to investigate any general effects disrupting the packing between these helices may have on this family. Interestingly the Thr87Asp variant also resulted in an increase in the rate of peptide transport, whereas other variants Thr87Ala/Ser/Lys showed WT like rates (Extended Data Fig. 9b-d) showing this region is sensitive to the addition of a negative charge. Comparable to what we observed for *At*NRT1.1, the Thr87Asp variant was also less stable than WT protein by 4 °C (Extended Data Fig. 9e). However a Thr87Arg variant was inactive suggesting gross structural distortion in this region cannot be tolerated. This shows that disrupting the helix packing between TMs 1, 3 and 4 in the N-terminal bundle of the NRT1/PTR family can dramatically affect transport rates. Similar studies have shown that altering the structural flexibility within the MFS fold can affect the rate-limiting step of transport [3334]. We propose a similar mechanism may occur in *At*NRT1.1 to switch the protein between a high and low Km state. Phosphorylation causes a localized disruption of the N terminal bundle helices that leads to an increased flexibility of the protein. This in turn leads to an increase in the transport rate, that would result in the lower Km observed in the previous study [24].

Model for proton coupled nitrate transport via *At*NRT1.1

Taken together a working model for proton coupled nitrate transport emerges from our study (Fig. 4). The protonation of His356 is clearly a key component of the transport mechanism. Our model predicts that protonation must occur prior to nitrate binding and may be conditional upon the presence of nitrate to stabilize the charged state of His356. Following closure of the extracellular gate and adoption of the occluded state the release of both proton and nitrate from His356 must be coupled to the opening of the intracellular gate. A possible mechanism in achieving this is that adoption of the occluded state brings His356 into close proximity to Glu476 causing the disruption of the intracellular gate salt bridge (Extended Data Fig. 7). The interaction between His356 and Glu476 may be facilitated by Tyr388

(TM8), which can be seen making a hydrogen bond to Glu476 in the crystal structures. The binding of additional protons potentially to the ExxERF motif might also affect the strength of the salt bridge between Lys164 and Glu476 facilitating opening of the intracellular gate and release of bound nitrate and protons into the interior of the cell. Our data suggest that in *At*NRT1.1 the effect of phosphorylation is to cause a localized disruption in the N-terminal bundle that in turn may affect the position of the ExxERF motif with respect to Lys164. The increase in transport rate that occurs is possibly the result of altering the efficiency in the formation and breakage of the Lys164-Glu476 salt bridge and release of nitrate from the binding site. Perhaps the most surprising finding from our study however is that only minor changes to the previously characterized peptide transporter binding site are required to accommodate nitrate and that these are predominantly located in the C-terminal bundle. The ability of the PTR family to recognize multiple ligands may therefore stem from the separation of a fundamentally conserved proton coupling mechanism that resides largely in the N-terminal bundle and orchestrates gross conformational changes between TMs4-5 and 10-11, whilst leaving the C-terminal bundle to evolve to recognize different nitrogenous ligands.

Methods

Cloning, Expression and Purification of *At*NRT1.1

The gene encoding *At*NRT1.1 was amplified from an Arabidopsis image clone and cloned into a modified form of a C-terminal GFP^{His} fusion yeast expression vector [35]. The yeast vector had an additional selection marker the LEU2 gene under the control of a truncated promoter to increase copy number within *Saccharomyces cerevisiae* [36]. Wild type and mutant *At*NRT1.1 were expressed by growing an overnight in minus leucine with 2 % glucose, this culture was diluted 10 fold in minus leucine with 2 % lactate, after 8-10 hours expression was induced thorough the addition of 2 % galactose from a 25 % stock. The yeast was harvested after 20 hours and membranes were prepared. *At*NRT1.1 and mutants were purified to homogeneity using standard IMAC protocols in n-dodecyl- β-D-maltopyranoside (DDM) detergent as described previously [37]. For MST binding experiments the C-terminal GFP^{His} was not removed. The protein was concentrated to 10 $mg.ml^{-1}$ for crystallization or 0.5 $mg.ml^{-1}$ for binding assays and stored at −80°C.

Crystallization and Structure Determination

Crystals of *At*NRT1.1 were initially obtained in the MemGold crystallization screen [38] and optimized to 22 % PEG 400, 0.05 M sodium citrate pH 4.5, 0.07 M sodium chloride and 1.5 % PEG 600 using the hanging drop vapor diffusion technique at 4 °C. For cryoprotection the crystals were transferred to a solution containing 33 % PEG 400, before being flash cooled in liquid nitrogen. The crystals always showed anisotropic diffraction, with the best crystals diffracting X-rays to Bragg spacing's of 3.50 Å in the strongest direction. Initial phases were calculated using single wavelength anomalous dispersion (SAD) using a single gold cyanide derivatised crystal. Data were collected on beamlines IO2, IO3, IO4 and IO4-1 at the Diamond Light Source Ltd., UK. Data were processed by the XIA2 [39,40] pipeline to XDS [41] and scaled using AIMLESS [42]. Diffraction data were collected to 3.5 Å (nitrate bound) and 3.6 Å (apo) resolutions and this data was used for calculating maps during model building however the final deposited model was refined against the 3.7 Å data shown in Extended Data Table 1, as the I/σI and completeness of the data dropped significantly after this resolution cut off. The space group was determined to be $P2_12_12_1$ with two molecules in the asymmetric unit forming a back to back dimer (Supp. Fig. 7). Two gold sites were initially located using SHELXC/D [43] with their positions further refined and initial phases calculated using SHARP with solvent flattening in SOLOMON [44]. The resulting experimental maps were of sufficient quality to see all 12 trans membrane helices from each of the two

molecules (Supp. Fig. 9). Further improvement in map quality was obtained following cross crystal averaging in DMMulti [45,46] with the native dataset. The lateral helix appeared in the maps following model building and refinement.

Model building and refinement

The model was built into experimental maps calculated from SHARP and DMMulti, using O [47]. The partial models were further cycled back into SOLOMON to improve the initial solvent envelope used for the solvent flipping procedure. The amino acid side chains were then built using an homology model of *At*NRT1.1 built from the template of $PepT_{St}$ (4APS) and GkPOT (4IKV) using modeller v9.12 [48]. Refinement of the model was carried out in BUSTER [49] with inclusion of experimental phase information. Model validation was carried out using the Molprobity server [50]. Images were prepared using PyMol [51].

Microscale thermophoresis binding assay

Binding was calculated for *At*NRT1.1 and the control POT family transporter, PepTSo [14], using microscale thermophoresis [26]. A range of concentrations of the required ligand (range from 0.1 μM to 50 mM) was incubated with 0.8 μM of purified GFP tagged protein 5 minutes in assay buffer (20 mM Bis-Tris pH 6.5, 150 mM NaCl, 0.03 % DDM). The sample was loaded into the NanoTemper glass capillaries and microthermophoresis carried out using 10 % LED power and 80 % MST. K_Ds were calculated using the mass action equation via the NanoTemper software from duplicate reads of triplicate experiments. The instrument used was a NanoTemper monolith NT.115.

$PepT_{So}$ transport assays using a proton driven proteoliposome system

$PepT_{So}$ was purified as previously described [14] and reconstituted by the dilution method. The efficiency of reconstitution was analysed by densitometry of a fixed amount of proteoliposomes using a serial dilution of purified protein as a standard. For proton driven uptake assays, artificially imposed potassium ion diffusion potentials were generated as previously described [52]. Proteoliposomes were thawed and centrifuged at 90,000 g for 30 min at 4 °C and re-suspended in 20 mM Potassium Phosphate, pH 6.50, 100 mM Potassium Acetate, 2mM Magnesium Sulfate, followed by 11 cycles of extrusion through a 400 nm polycarbonate filter to obtain small unilamellar vesicles of relatively homogenous size [53]. Proteoliposomes were subsequently diluted 1:50 (v/v) to final protein concentration of 0.25 μM into external buffer containing 20 mM Na Phosphate, pH 6.5, 2 mM magnesium sulphate with 10 μM valinomycin and ^{3}H-labeled di-Ala peptide (40 μM). Uptake of ^{3}H substrate was assayed at 25 °C. Diluting aliquots into 1.5 ml of ice-cold 0.1 M lithium chloride stopped the reaction. Proteoliposomes were collected on 0.22 μm nitrocellulose filters and washed under vacuum with 0.1 M Lithium Chloride prior to scintillation counting. The ^{3}H signal was converted to molar concentrations of peptide using standard curves for each substrate.

Reconstitution of *At*NRT1.1 into liposomes

*At*NRT1.1 was reconstituted into liposomes using the biobead method. Polar soy lipids (Avanti polar lipids) were washed twice in pentane and resuspended at 5 mg/ml in lipid buffer (50 mM potassium phosphate pH 7.5). The lipids were extruded through a 0.4 μm filter and titrated with Triton X-100 until the absorbance at 540 nm was ~90% of maximal. Purified *At*NRT1.1 (0.2 mg) was added to the lipids at a final lipid:protein ratio of 60:1 and incubated for 1 hour on ice or for the no protein liposome control the same volume of gel filtration buffer used to purify *At*NRT1.1 was added. After this time the required amount of biobeads (~0.1 mg) were added and incubated at 4 °C with rotary mixing for 3 hours. The biobead addition was repeated a further three times with the final incubation being

Europe PMC Funders Author Manuscripts

overnight. The biobeads were removed and proteoliposomes were harvested by centrifugation at 120,000 g for 30 minutes. Proteoliposomes were resuspended in lipid buffer at a final lipid concentration of 30 μg/μl and dialysed overnight in lipid buffer to remove any traces of residual detergent. After dialysis the proteoliposomes were harvested and resuspended as before and subjected to three rounds of freeze thawing in liquid nitrogen before storage at −80 °C. Protein amount was quantified by SDS-PAGE and densitometry.

Nitrate transport assays using pyranine dye

*At*NRT1.1 proteoliposomes were thawed and harvested at by centrifugation at 120,000g for 25 minutes at 4 °C. The liposomes were resupended in inside buffer (5 mM Hepes pH 6.8, 120 mM KCl, 2 mM $MgSO_4$) and 1 mM pyranine and loaded by two rounds of freeze thawing in liquid nitrogen followed by extrusion through first a 0.4 μm filter then a 0.2 μm filter. Excess pyranine was removed by washing once in inside buffer and then by application to a G25 gel filtration (GE Healthcare) column equilibrated in inside buffer. After this step the liposomes were split into 8 μg aliquots (enough for one assay per tube) and harvested by centrifugation at 120,000 g for 25 minutes at 15 °C.

The prepared liposomes were resuspended in 99 ul external buffer (5 mM MES pH 6.0, 1 mM KCl, 2 mM $MgSO_4$, 109 mM NaCl) and immediately the fluorescence was read at 460/510 and 415/510 in a SpectraMax M3 plate reader using 96 well black clear bottom plates (Molecular Devices). Each assay was measured individually. Either 10 mM sodium nitrate or 10 mM sodium chloride (no nitrate control) from 1 M stocks were added and again fluorescence read immediately after the addition and mixing. Data were collected for 30 seconds in 10-second increments. The difference between nitrate and no nitrate after 20 seconds was calculated (averaged from 8 experiments) and used to compare the variants of *At*NRT1.1 (data shown in figure 3B).

Supplementary Material

Refer to Web version on PubMed Central for supplementary material.

Acknowledgments

We wish to thank Dr Ralf Flaig, Diamond Light Source, Ltd, for help with additional access to beamline IO4. This research was funded through the Medical Research Council (MRC) Career Development Award grant G0900399 and Royal Society grants (RG110211 & IE111401) to SN.

References

1. Steiner H-Y, Naider F, Becker JM. The PTR family: a new group of peptide transporters. Mol Microbiol. 1995; 16:825–834. [PubMed: 7476181]
2. Daniel H, Spanier B, Kottra G, Weitz D. From bacteria to man: archaic proton-dependent peptide transporters at work. Physiology. 2006; 21:93–102. [PubMed: 16565475]
3. Crawford NM. Nitrate: nutrient and signal for plant growth. Plant Cell. 1995; 7:859–868. [PubMed: 7640524]
4. Tsay, YF.; Hsu, PK. The Plant Plasma Membrane. Vol. 19. Springer; Berlin Heidelberg: 2010. p. 223-236.Plant Cell Monographs
5. Orsel M, et al. Characterization of a Two-Component High-Affinity Nitrate Uptake System in Arabidopsis. Physiology and Protein-Protein Interaction. Plant Physiol. 2006; 142:1304–1317. [PubMed: 17012411]
6. Dechorgnat J, et al. From the soil to the seeds: the long journey of nitrate in plants. Journal of Experimental Botany. 2011; 62:1349–1359. [PubMed: 21193579]

7. Tsay YF, Schroeder JI, Feldmann KA, Crawford NM. The herbicide sensitivity gene CHL1 of Arabidopsis encodes a nitrate-inducible nitrate transporter. Cell. 1993; 72:705–713. [PubMed: 8453665]
8. Forde B, Gassmann W, Geiger D, Gojon A. A unified nomenclature of nitrate transporter 1/peptide transporter family members in plants. Trends in plant Science. 2013; 19:5–9. [PubMed: 24055139]
9. Tsay Y-F, Chiu C-C, Tsai C-B, Ho C-H, Hsu P-K. Nitrate transporters and peptide transporters. FEBS Lett. 2007; 581:2290–2300. [PubMed: 17481610]
10. Boursiac Y, et al. ABA transport and transporters. Trends in Plant Science. 2013; 18:325–333. [PubMed: 23453706]
11. Nour-Eldin HH, Andersen TG, Burow M, Madsen SR. NRT/PTR transporters are essential for translocation of glucosinolate defence compounds to seeds. Nature. 2012; 488:531–534. [PubMed: 22864417]
12. Krouk G, et al. Nitrate-Regulated Auxin Transport by NRT1.1 Defines a Mechanism for Nutrient Sensing in Plants. Developmental Cell. 2010; 18:927–937. [PubMed: 20627075]
13. Reddy VS, Shlykov MA, Castillo R, Sun EI, Saier MH. The major facilitator superfamily (MFS) revisited. FEBS Journal. 2012; 279:2022–2035. [PubMed: 22458847]
14. Newstead S, et al. Crystal structure of a prokaryotic homologue of the mammalian oligopeptide-proton symporters, PepT1 and PepT2. EMBO J. 2011; 30:417–426. [PubMed: 21131908]
15. Fei YJ, et al. Expression cloning of a mammalian proton-coupled oligopeptide transporter. Nature. 1994; 368:563–566. [PubMed: 8139693]
16. Nakajima H, et al. Cloning and functional expression in Escherichia coli of the gene encoding the di- and tripeptide transport protein of Lactobacillus helveticus. Appl Environ Microbiol. 1997; 63:2213–2217. [PubMed: 9172341]
17. Chiang C-S, Stacey G, Tsay Y-F. Mechanisms and functional properties of two peptide transporters, AtPTR2 and fPTR2. J Biol Chem. 2004; 279:30150–30157. [PubMed: 15138259]
18. Radestock S, Forrest LR. The alternating-access mechanism of MFS transporters arises from inverted-topology repeats. Journal of Molecular Biology. 2011; 407:698–715. [PubMed: 21315728]
19. Yan N. Structural advances for the major facilitator superfamily (MFS) transporters. Trends Biochem Sci. 2013; 38:151–159. [PubMed: 23403214]
20. Madej MG, Dang S, Yan N, Kaback HR. Evolutionary mix-and-match with MFS transporters. Proc Natl Acad Sci U S A. 2013; 110:5870–5874. [PubMed: 23530251]
21. Solcan N, et al. Alternating access mechanism in the POT family of oligopeptide transporters. EMBO J. 2012; 31:3411–3421. [PubMed: 22659829]
22. Doki S, et al. Structural basis for dynamic mechanism of proton-coupled symport by the peptide transporter POT. Proc Natl Acad Sci U S A. 2013; 110:11343–11348. [PubMed: 23798427]
23. Liu KH, Huang CY, Tsay YF. CHL1 is a dual-affinity nitrate transporter of Arabidopsis involved in multiple phases of nitrate uptake. Plant Cell. 1999; 11:865–874. [PubMed: 10330471]
24. Liu K-H, Tsay Y-F. Switching between the two action modes of the dualaffinity nitrate transporter CHL1 by phosphorylation. EMBO J. 2003; 22:1005–1013. [PubMed: 12606566]
25. Wang Y-Y, Hsu P-K, Tsay Y-F. Uptake, allocation and signaling of nitrate. Trends in Plant Science. 2012; 17:458–467. [PubMed: 22658680]
26. Baaske P, Wienken C, Willemsen MJ, Braun D. Protein-Binding Assays in Biological Liquids Using Microscale Thermophoresis. Journal of Biomolecular Techniques. 2011; 22:S55.
27. Wienken CJ, Baaske P, Rothbauer U, Braun D. Protein-binding assays in biological liquids using microscale thermophoresis. Nature Communications. 2010; 1:100.
28. Sun L, et al. Crystal structure of a bacterial homologue of glucose transporters GLUT1-4. Nature. 2012; 490:361–366. [PubMed: 23075985]
29. Dang S, et al. Structure of a fucose transporter in an outward-open conformation. Nature. 2010; 467:734–738. [PubMed: 20877283]
30. Guettou F, et al. Structural insights into substrate recognition in proton-dependent oligopeptide transporters. EMBO Rep. 2013; 14:804–810. [PubMed: 23867627]

31. Yan H, et al. Structure and Mechanism of a Nitrate Transporter. Cell Rep. 2013; 3:716–723. [PubMed: 23523348]
32. Mackenzie B, et al. Mechanisms of the human intestinal H+-coupled oligopeptide transporter hPEPT1. J Biol Chem. 1996; 271:5430–5437. [PubMed: 8621398]
33. Chandrasekaran A, Ojeda AM, Kolmakova NG, Parsons SM. Mutational and bioinformatics analysis of proline- and glycine-rich motifs in vesicular acetylcholine transporter. J Neurochem. 2006; 98:1551–1559. [PubMed: 16923166]
34. Ugolev Y, Segal T, Yaffe D, Gros Y, Schuldiner S. Identification of Conformationally Sensitive Residues Essential for Inhibition of Vesicular Monoamine Transport by the Noncompetitive Inhibitor-Tetrabenazine. J. Biol. Chem. 2013; 288:32160–32171. [PubMed: 24062308]
35. Newstead S, et al. High-throughput fluorescent-based optimization of eukaryotic membrane protein overexpression and purification in Saccharomyces cerevisiae. Proc Natl Acad Sci USA. 2007; 104:13936–13941. [PubMed: 17709746]

Supplementary References

36. Kazemi Seresht A, Nørgaard P, Palmqvist EA, Andersen AS, Olsson L. Modulating heterologous protein production in yeast: the applicability of truncated auxotrophic markers. Appl. Microbiol. Biotechnol. 2013; 97:3939–3948. [PubMed: 22782252]
37. Drew D, et al. GFP-based optimization scheme for the overexpression and purification of eukaryotic membrane proteins in Saccharomyces cerevisiae. Nature Protocols. 2008; 3:784–798.
38. Newstead S, Ferrandon S, Iwata S. Rationalizing alpha-helical membrane protein crystallization. Protein Sci. 2008; 17:466–472. [PubMed: 18218713]
39. Winter G, Lobley CMC, Prince SM. Decision making in xia2. Acta Crystallogr D Biol Crystallogr. 2013; 69:1260–1273. [PubMed: 23793152]
40. Winter G. xia2: an expert system for macromolecular crystallography data reduction. Journal of Applied Crystallography. 2009; 43:186–190.
41. Kabsch W. XDS. Acta Crystallogr D Biol Crystallogr. 2010; 66:125–132. [PubMed: 20124692]
42. Evans PR. An introduction to data reduction: space-group determination, scaling and intensity statistics. Acta Crystallogr D Biol Crystallogr. 2011; 67:282–292. [PubMed: 21460446]
43. Sheldrick GM. Experimental phasing with SHELXC/ D/ E: combining chain tracing with density modification. Acta Crystallogr D Biol Crystallogr. 2010; 66:479–485. [PubMed: 20383001]
44. Abrahams JP, Leslie AGW. Methods used in the structure determination of bovine mitochondrial F1 ATPase. Acta Crystallogr D Biol Crystallogr. 1996; 52:30–42. [PubMed: 15299723]
45. DM′: an automated procedure for phase improvement by density modification. Joint CCP4 and ESF-EACBM Newsletter on Protein Crystallography. 31:34–38.
46. Pedersen BP, Morth JP, Nissen P. Structure determination using poorly diffracting membrane-protein crystals: the H +-ATPase and Na +,K +-ATPase case history. Acta Crystallogr D Biol Crystallogr. 2010; 66:309–313. [PubMed: 20179343]
47. Jones TA, Zou JY, Cowan SW, Kjeldgaard M. Improved methods for building protein models in electron density maps and the location of errors in these models. Acta Crystallogr, A, Found Crystallogr. 1991; 47(Pt 2):110–119.
48. Yang Z, et al. UCSF Chimera, MODELLER, and IMP: An integrated modeling system. J. Struct. Biol. 2011; 179:269–278. [PubMed: 21963794]
49. Blanc E, et al. Refinement of severely incomplete structures with maximum likelihood in BUSTER-TNT. Acta Crystallogr D Biol Crystallogr. 2004; 60:2210–2221. [PubMed: 15572774]
50. Davis IW, Murray LW, Richardson JS, Richardson DC. MOLPROBITY: structure validation and all-atom contact analysis for nucleic acids and their complexes. Nucleic Acids Res. 2004; 32:W615–9. [PubMed: 15215462]
51. Schrodinger LLC. The PyMOL Molecular Graphics System (Version 1.3r1).
52. Foucaud C, Poolman B. Lactose transport system of Streptococcus thermophilus. Functional reconstitution of the protein and characterization of the kinetic mechanism of transport. J Biol Chem. 1992; 267:22087–22094. [PubMed: 1429561]

53. Knol J, et al. Unidirectional reconstitution into detergent-destabilized liposomes of the purified lactose transport system of Streptococcus thermophilus. J Biol Chem. 1996; 271:15358–15366. [PubMed: 8662938]

54. Smirnova I, et al. Sugar binding induces an outward facing conformation of LacY. Proc Natl Acad Sci USA. 2007; 104:16504–16509. [PubMed: 17925435]

55. Zheng H, Wisedchaisri G, Gonen T. Crystal structure of a nitrate/nitrite exchanger. Nature. 2013; 497:647–651. [PubMed: 23665960]

Europe PMC Funders Author Manuscripts

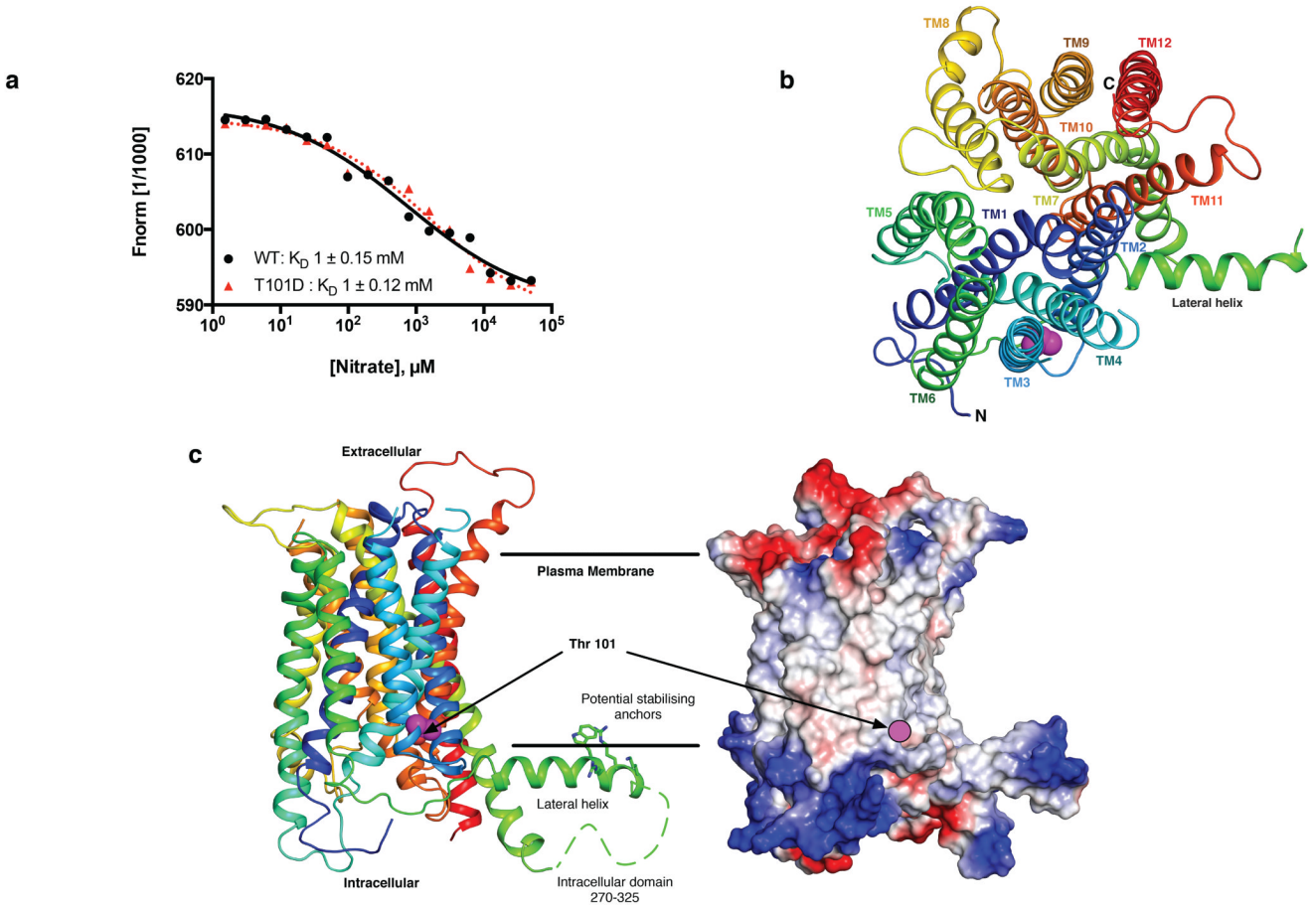

Figure 1. Structural and biophysical characterisation of *At*NRT1.1

a. Binding isotherms for nitrate to both wild type (black squares) and T101D (red triangles) reveals no significant change in the K_D. Data shown is representative of three independent experiments and the error is calculated as standard deviation. b. Cartoon representation of the crystal structure of *At*NRT1.1 viewed from the extracellular side of the plasma membrane. Transmembrane helices (TM) 1-12 have been coloured from blue at the amino terminus to red at the carboxy terminus. T101 is shown as magenta spheres. c. *At*NRT1.1 viewed in the plane of the membrane represented as both cartoon and electrostatic surface, positively charged and aromatic residues at the end of the lateral helix are shown in sticks and may help to anchor this helix in the interfacial region of the plasma membrane. Residues 270-325 of the intracellular domain could not be modeled due to insufficient electron density.

Europe PMC Funders Author Manuscripts

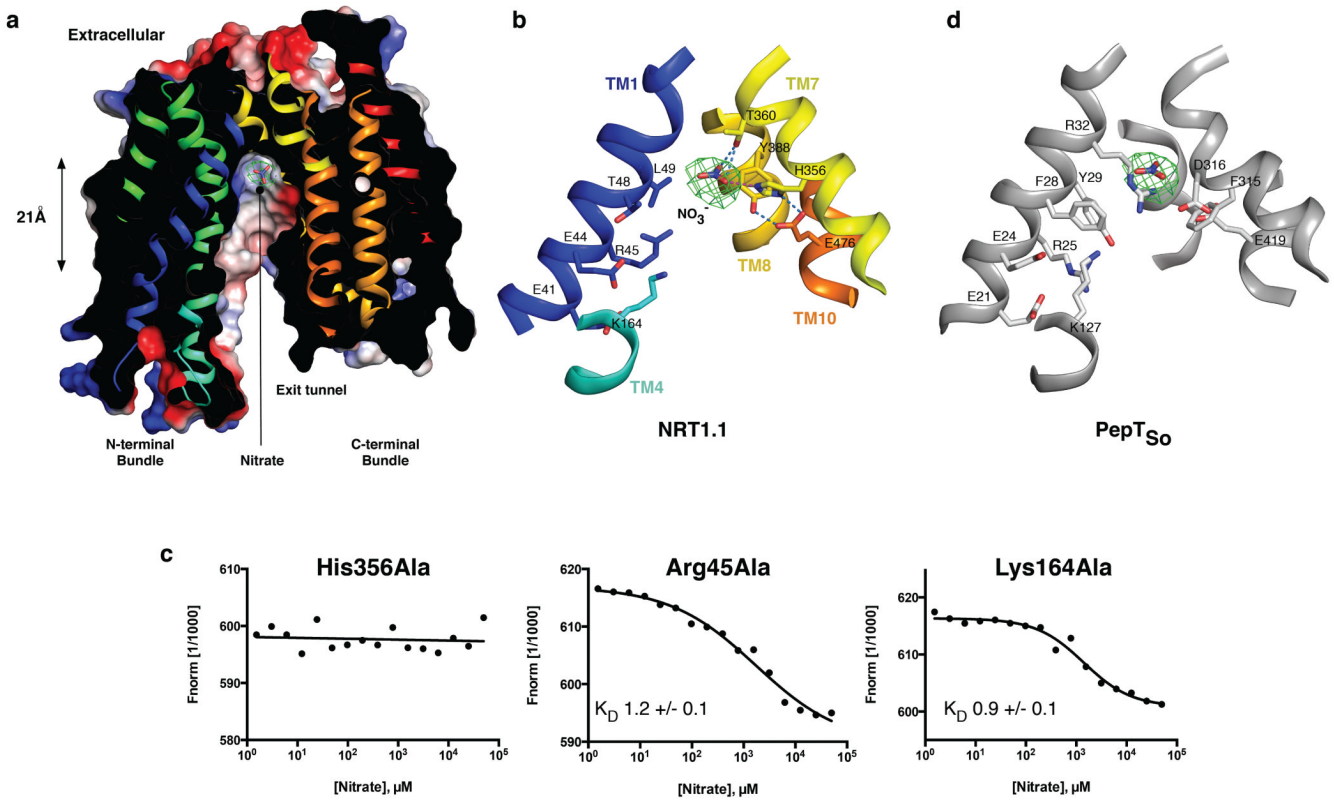

Figure 2. Crystal structure of nitrate bound *At*NRT1.1

a. A section through the protein volume showing the binding site in the plane of the membrane, with the mFo-DFc difference electron map contoured at 3 sigma (green) identifying the position of nitrate. b. Zoomed in view of the binding site. Shown in sticks are the conserved PTR/NRT1 residues and His356 that can be seen coordinating nitrate within the binding site, supported by Thr360. Dashed lines indicate a potential interaction network between His356, Tyr388 and Glu476 in the C-terminal bundle. c. Binding isotherms showing the effect of mutating positively charged residues in the binding site on the affinity of *At*NRT1.1 for nitrate. Data shown is representative of three independent experiments and the error is calculated as standard deviation. d. Similarity between the binding sites of the peptide transporter $PepT_{So}$ and *At*NRT1.1. Shown in sticks are the residues important for peptide transport. The relative position of nitrate from the *At*NRT1.1 structure is superimposed (green mesh).

Europe PMC Funders Author Manuscripts

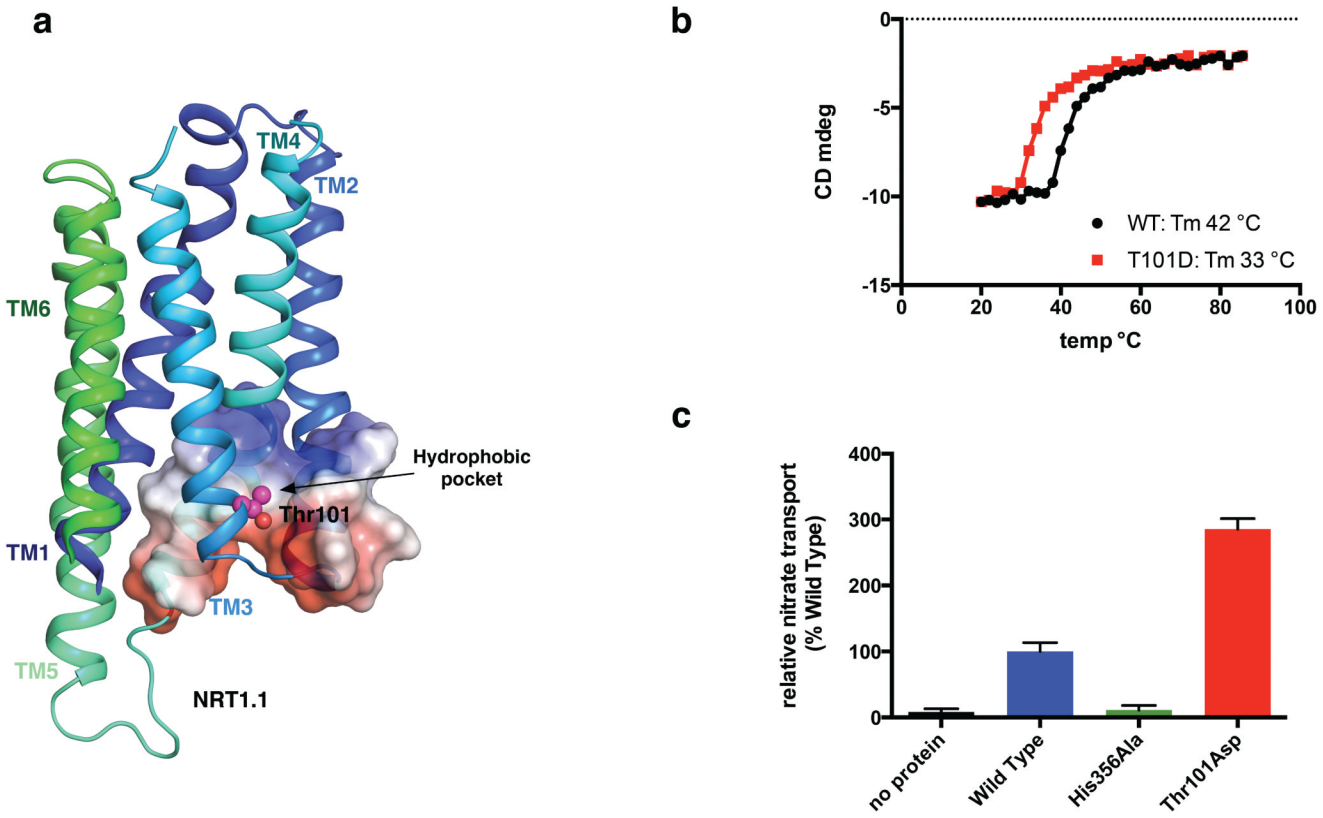

Figure 3. Proposed mechanism for the affect of phosphorylation at Thr101 on nitrate transport

a. Thr101 (represented as magenta spheres) in *At*NRT1.1 is situated in a hydrophobic cavity formed at the intracellular ends of TMs 2 and 4. b. Thermal stability as assessed by the loss of alpha helical secondary structure using circular dichroism shows a reduction in the Thr101Asp variant when compared to wild type protein. c. The Thr101Asp variant of *At*NRT1.1 shows a significant increase in transport when compared to wild type protein in a reconstituted assay system, where as the His356Ala mutant shows no activity. Data represents the mean value from eight experiments and error bars are standard deviation.

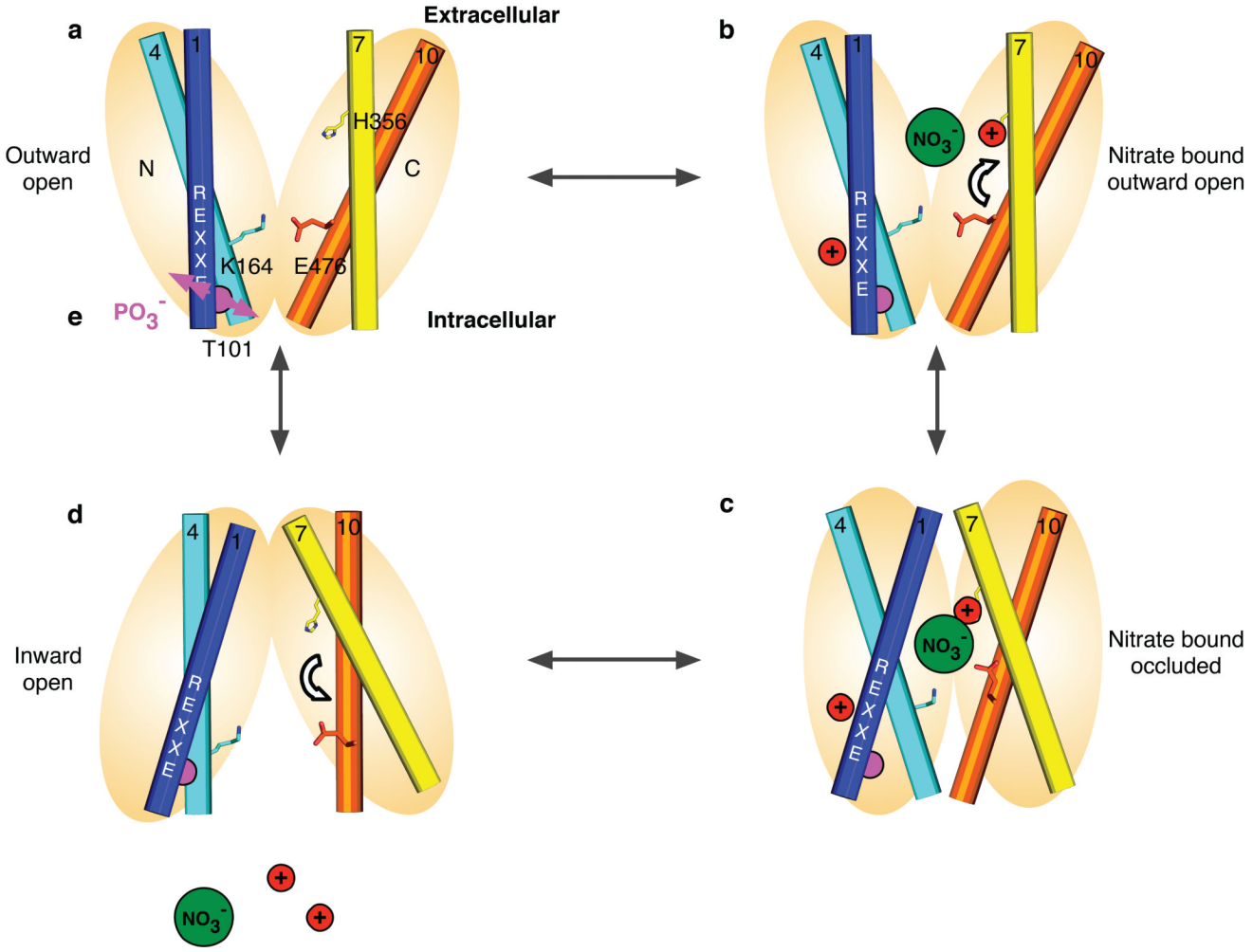

Figure 4. Alternating access model for nitrate-proton symport

In the outward facing state (a) the extracellular gate, constructed from TMs1-2 (dark blue) and TMs7-8 (yellow) is open and the intracellular gate, constructed from TM4-5 (cyan) packing against TM10-11 (orange) is closed and stabilized by a salt bridge between Lys164 (TM4) and Glu476 (TM10) - similar to the bacterial homologues. Following protonation of His356, nitrate is able to bind triggering closure of the extracellular gate (b). Additional sites of protonation exist possibly within the ExxERF motif (TM1). Upon transition to the occluded state (c) the intracellular gate salt bridge will break as a result of Glu476 moving to form a new salt bridge with His356. This will result in the release of nitrate and protons into the interior of the cell (d). Phosphorylation of Thr101 (purple sphere) by CIPK23 results in increased flexibility within the N-terminal bundle, increasing the overall transport rate (e).

Europe PMC Funders Author Manuscripts